



Establishing a high-speed electron transfer channel via CuS/MIL-Fe heterojunction catalyst for photo-Fenton degradation of acetaminophen

Zhimo Fang^a, Yibo Liu^b, Juanjuan Qi^{a,*}, Zhong-Fei Xu^a, Tiejue Qi^{a,b}, Lidong Wang^{a,b,**}

^a The Key Laboratory of Resources and Environmental System Optimization, Ministry of Education; College of Environmental Science and Engineering, North China Electric Power University, Beijing 102206, China

^b The Hebei Key Laboratory of Power Plant Flue Gas Multi-Pollutants Control, Department of Environmental Science and Engineering, North China Electric Power University, Baoding 071003, PR China

ARTICLE INFO

Keywords:

Photo-Fenton
Electron transfer
DFT calculation
Heterointerface
CuS/MIL-Fe

ABSTRACT

Active pharmaceutical pollution has become “a new force” of water pollution, and a high-efficiency process is urgently required to remove it. Herein, the CuS/MIL-Fe heterojunction catalyst with high-speed electron transfer channel is designed by adjusting the energy band and regulating the direction of electron transfer, which exhibits excellent acetaminophen (APAP) removal ability in photo-Fenton reaction. The charge transfer pathway of heterojunction is identified by X-ray photoelectron spectroscopy analysis and density functional theory (DFT) calculation, which provides the evidence of electron transfer from CuS to MIL-101(Fe) at the heterointerface. Meanwhile, kelvin probe force microscopy measurement indicates that photogenerated electrons can be easily transported through the CuS/MIL-Fe interface. The close contact interface and high charge transfer conductivity realize the synergistic effect of photo and Fenton degradation by establishing high-speed electron transfer channel. This study will open up a new insight into the application of heterojunction photo-Fenton technology in environmental remediation.

1. Introduction

Over the past few decades, the extensive application and even abuse of pharmaceuticals and personal care products (PPCPs) have led to their widespread existence in the global water environment, which has become one of the water pollution problems confronted by all mankind [1]. Among the PPCPs, acetaminophen (APAP) is one of the most widely used antipyretic and analgesic drugs in all the nations [2]. A large amount of APAP is released into water during the pharmaceutical process and human metabolism [3], which is difficult to be removed by traditional sewage treatment process [4]. Therefore, it is urgent to establish an effective treatment technology to remove APAP.

Currently, Fenton technology is the most widely used advanced oxidation process for sewage purification [5–7]. However, the traditional Fenton technology faces challenges such as narrow pH application range, low H₂O₂ utilization rate, and secondary pollution caused by Fe-based sludge [8]. Heterogeneous photo-Fenton process has attracted the attention of the public because of its advantages of environmental

friendliness and high efficiency [9]. The technology not only makes rational use of green solar energy, realizes efficient decomposition of H₂O₂, and avoids sludge [10]. The photo-Fenton technology enables Fenton reagent to cooperate with light irradiation to achieve effective degradation of APAP by constructing a high-speed electron transfer channel. The synergistic effect promotes the faster decomposition of H₂O₂ to produce reactive oxygen species (ROS) including hydroxyl (•OH), superoxide radicals (•O₂⁻), singlet oxygen superoxide (¹O₂), and photo-generated holes (h⁺) to ensure the pollutant removal efficiency [11]. However, the application of assorted photo-Fenton catalysts is hampered by the disadvantages of the limited pH conditions, the difficult recovery, and the easy recombination of photogenerated electrons (e⁻) and holes (h⁺) [12]. Hence, it is expected to break through the technical bottleneck by constructing an efficient photo-Fenton catalyst.

Metal organic frameworks (MOFs) are brought into sharp focus due to their high porosity, adjustable active center, and easy functional modification [13,14]. Materials of Institute Lavoisier (MILs) have a high specific surface area and porosity, which makes it easier to expose the

* Corresponding author.

** Corresponding author at: The Key Laboratory of Resources and Environmental System Optimization, Ministry of Education; College of Environmental Science and Engineering, North China Electric Power University, Beijing 102206, China.

E-mail addresses: qijuanjuan@ncepu.edu.cn (J. Qi), wld@ncepu.edu.cn (L. Wang).

<https://doi.org/10.1016/j.apcatb.2022.121979>

Received 26 July 2022; Received in revised form 26 August 2022; Accepted 10 September 2022

Available online 16 September 2022

0926-3373/© 2022 Elsevier B.V. All rights reserved.

active metal sites during the reaction process [15,16]. Therefore, iron-containing MIL-101 (MIL-101(Fe), a typical *n* semiconductor) have the advantage of promoting the regeneration of Fe due to the complexation of the carboxyl group to iron in their structure, which is considered to be a promising Fenton reaction material [17]. However, the MIL-101(Fe) still exhibits low photocatalytic behavior owing to the recombination of photogenerated e^- and h^+ [18]. It is obliged to combine MIL-101(Fe) with a suitable semiconductor to construct heterojunction to improve the catalytic performance.

Copper sulfide (CuS) is a typical *p* semiconductor with available and earth-abundant that has received great interest due to its unique optical and electrical properties [19,20]. Chen et al. [21] found that $BaSO_4$ -CuS heterostructure had excellent optical properties to promote charge separation, thus accelerating tetracycline degradation. Lai et al. [22] proposed that $CuS/BiVO_4$ as a *p-n* heterojunction photocatalyst had excellent photocatalytic efficiency to degrade ciprofloxacin. The introduction of semiconductor to construct heterojunction catalyst into Fenton reaction would generate photo-generated electron under light radiation. An electron transfer channel was formed to continuously input electron from photodegradation into Fenton reaction, and CuS could also be used as electron donors, both of which can accelerate the redox process of Fe. Therefore, two matched semiconductors are coupled to form a *p-n* heterojunction structure, and a high-speed electron transfer channel is constructed to connect the two reaction centers, which is conducive to improve the properties of photo-Fenton reaction.

Herein, we have designed a novel CuS-modified MIL-101(Fe) (named as CuS/MIL-Fe) heterojunction catalyst via a facile solvothermal strategy. Experimental, characterization, and DFT have effectively proved that the strong interface interaction of CuS/MIL-Fe can effectively separate space charges, thus promoting the decomposition of H_2O_2 to generate a large number of ROS through the built-in redox couple (Fe, Cu, and S) in CuS/MIL-Fe. CuS/MIL-Fe constructs a high-speed electron transfer channel as a bridge to realize the synergistic effect of photodegradation and Fenton degradation. As expected, the as-prepared CuS/MIL-Fe heterojunction shows a robust performance of the APAP photo-Fenton degradation.

2. Experimental

2.1. Catalyst synthesis

All the chemicals were purchased commercially and used without further purification, which were described in Text S1 in the Supporting Information (SI). The details of catalyst preparation were described in Text S2. All the characterization methods are detailed in Text S3.

2.2. Photo-Fenton activity evaluation

The photo-Fenton performances of as-prepared catalysts were measured under a simulated solar irradiation by a 300 W Xenon lamp (CELPE3⁰⁰L-³A) and the reaction temperature of 25 °C. 10 mg catalyst was added into 100 mL APAP solution (5 mg·L⁻¹). After dark stirring for 30 min, 10 mM H_2O_2 (30%) was added to start the reaction. At pre-determined time, 1.5 mL of analytical sample was drawn from reaction solution and 100 μ L of 0.1 M $Na_2S_2O_3$ solution was then add quickly to terminate the photo-Fenton reaction. The effect of experimental factors, including pH and various anions, was investigated. Diluted NaOH and HCl solutions (0.1 mM) were used to adjust the initial pH values at 3, 5, 7, 9, and 11, respectively. During the process of the cycling experiment, CuS/MIL-Fe was recycled using vacuum filtration, dried at 60 °C, and used in the next experiment without any further treatment.

2.3. Analytical methodology

High-performance liquid chromatography (HPLC) is used to analyze the concentration of APAP and liquid chromatography-mass

spectrometry (LC-MS) is used to determine the intermediate products of APAP. The reaction rate of APAP is evaluated by the *pseudo*-first-order kinetic model. The relevant methods are detailed in Text S4. The residual H_2O_2 concentration detection method is detailed in Text S5. The theoretical calculation method using Spin-polarized Density Functional Theory (DFT) calculations is detailed in Text S6.

3. Results and discussion

3.1. Characterization

CuS/MIL-Fe composites were prepared by two-step solvothermal method, as shown in Fig. 1a. Fig. S1 implied that the scanning electron microscope (SEM) image of MIL-101(Fe). MIL-101(Fe) was found to grow into spindle rod shape after secondary hydrothermal reaction in Fig. 1b. Previous studies have reported that secondary hydrothermal processes can lead to structural rearrangements and morphological changes [23,24]. We conducted hydrothermal treatment on MIL-101(Fe) alone. Fig. S1c exhibited that the morphology of the catalyst changed from flat to concave but still possessed the octahedral structure. Therefore, it was speculated that secondary hydrothermal process might not be crucial to affect the crystal growth of MIL-101(Fe). Besides, Zhang et al. reported that the preparation of MIL-101(Fe)- NH_2 (MIL-N) utilized 2-aminoterephthalic acid (NH_2 -TPA) as a ligand by solvothermal method, which possessed similar structure of MIL-101(Fe) in our composite CuS/MIL-Fe. By contrasting the morphologies after secondary hydrothermal, the morphology of MIL-101(Fe) alone was basically unchanged (Fig. S1) while the MIL-101(Fe) grew long in the CuS/MIL-Fe, which was attributed to the introduction of $Cu(NO_3)_2 \cdot 3H_2O$ and C_2H_5NS during the preparation of the composites. Further, by comparing with the synthesis method of MIL-101(Fe)- NH_2 [25], we found that the ligands were different, in which the preparation of NH_2 -TPA involved the nitrification and reduction of terephthalic acid (TPA) [26,27]. Therefore, we deduced that the morphology change of MIL-101(Fe) in CuS/MIL-Fe might be due to the effects of NO_3^- (nitrification) and C_2H_5NS (reduction) in secondary hydrothermal processes. CuS nanoparticles loaded around MIL-101(Fe) were also easily observed in Fig. 1c. In order to further understand the microstructure of CuS/MIL-Fe, the transmission electron microscopy (TEM) and high resolution TEM (HRTEM) were used to characterize CuS/MIL-Fe. It could be clearly observed that a distinct and stable interface was formed between CuS and MIL-101(Fe) (Fig. 1d and e), indicating the successful architecture of interface engineering [28]. The interplanar spacings were measured to be 0.32 and 0.19 nm (Fig. 1f and g), which conformed to be the (100) and (110) planes of the hexagonal CuS, respectively [29]. The corresponding elemental mapping of CuS/MIL-Fe composite was shown in Fig. 1h with Fe, Cu, S, C, and O elements. The above results preliminarily proved that CuS was successfully encapsulated on MIL-101(Fe) to form heterojunction.

X-ray diffraction (XRD) technology was used to measure the crystal phase types of as-prepared catalysts (Fig. 2a). For CuS, the characteristic peaks were observed at 27.6°, 29.2°, 31.9°, 47.9°, 52.8°, and 59.3°, ascribed to (101), (102), (103), (110), (108), and (116) planes, respectively, which corresponded to typical hexagonal structure of CuS covellite phase (JCPDS 06-0464). The characteristic peaks of as-prepared MIL-101(Fe) was in good agreement with simulated MIL-101(Fe) and other previous reports [30]. After coupling MIL-101(Fe) with CuS, some peak intensities of CuS and MIL-101(Fe) decreased or even disappeared, but the prominent peak was still retained, which was attributed to the decrease of CuS and MIL-101(Fe) content. This phenomenon was consistent with the reported literature [17,31,32]. These results were consistent with the observed crystal morphology shown in their SEM images.

The FT-IR spectra was used to confirm the framework vibration structures of catalysts (Fig. 2b). For MIL-101(Fe), the peak at 554 cm^{-1} could be considered to the Fe-O bond. The peaks at 748 and 1001 cm^{-1}

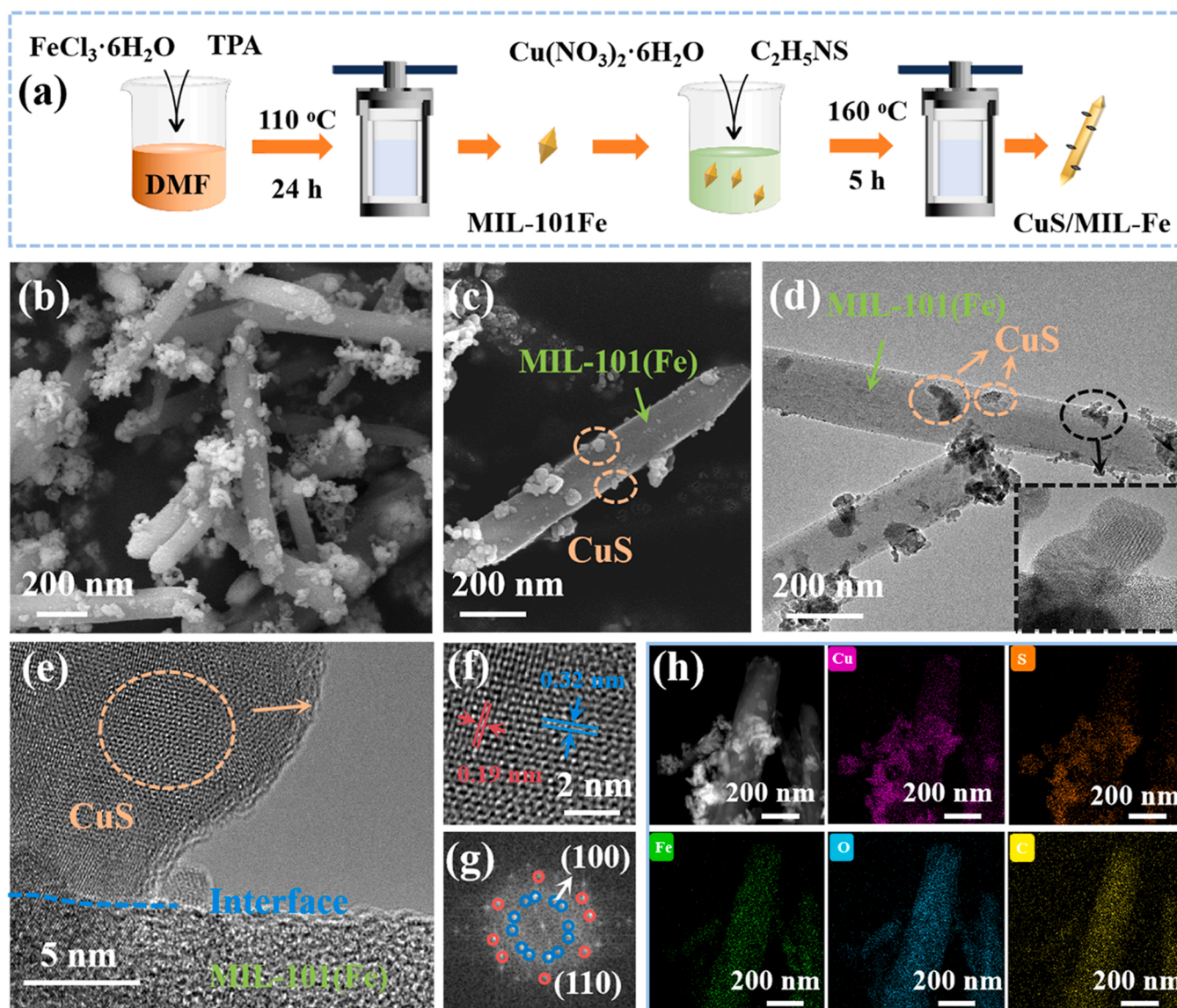


Fig. 1. (a) Schematic diagram of CuS/MIL-Fe synthesis process. (b, c) SEM, (d) TEM, and (e-f) HRTEM of CuS/MIL-Fe. (g) FFT pattern of CuS (h) Elemental mapping of CuS/MIL-Fe.

were C-H bond and C-O, which were related to the vibrations of the benzene ring structure. The peaks of 1389, 1504, and 1597 cm^{-1} were attributed to be the symmetric and asymmetric stretching of carboxyl groups in ligands. The signal at 1703 cm^{-1} was attributed to the stretching vibration of C=O [16]. For CuS, the peak of 621 cm^{-1} was attributed to Cu-S [33]. For CuS/MIL-Fe, a new small peak at 1250 cm^{-1} attributed to the C-N stretch was observed which indicated the aromatic amine functional group [34]. The formation of CuS/MIL-Fe heterojunction brought out the slightly weaker peak intensity of CuS/MIL-Fe than MIL-101(Fe) and CuS alone. The N₂ adsorption-desorption measurement, Brunauer-Emmett-Teller (BET) specific surface area, pore diameter and pore volume of as-prepared catalysts was shown in Fig. S2, and the specific analysis was in Text S7.

The ESR was applied to detect the concentration of defect in the as-prepared samples. As shown in Fig. 2c, all samples showed resonance signals at $g = 2.002$, among which the intensity of CuS/MIL-Fe signal was the strongest. For CuS and MIL-101(Fe) alone, the signal might be caused by the presence of S and ligand vacancies [35,36]. After recombination, the synergistic effect of vacancies caused the catalyst to produce more unpaired electrons, which could promote the electron transfer on the catalyst surface to improve the catalytic activity [37].

The XPS spectra were performed to investigate the surface chemical states and the electronic interaction between the surface elements of the catalysts. The XPS survey spectra of CuS, MIL-101(Fe), and CuS/MIL-Fe in Fig. S3a. Peaks of Cu, Fe, O, C, S, and N elements were observed, suggesting that these elements coexisted in the CuS/MIL-Fe. The Fe 2p XPS spectra of four peaks were provided in Fig. 2d. The peaks of Fe 2p_{3/2} were deconvoluted to three peaks at 710.1, 712.6 and 717.6 eV were attributed to Fe(II), Fe(III) and satellite, respectively. The peaks at 724.9, 727.5, and 732.8 eV belonged to Fe(II), Fe(III) and satellite of Fe 2p_{1/2} [38]. Fig. 2e showed the four peaks in the Cu 2p spectra of CuS and CuS/MIL-Fe. The peaks at 932.1 and 952.1 eV were ascribed to Cu(II) 2p_{3/2} and Cu(II) 2p_{1/2}, and the peaks at 933.5 and 954.6 eV were correspond to Cu(I) 2p_{3/2} and Cu(I) 2p_{1/2} [39]. Fig. 2f showed that the characteristic peaks at 161.9 and 163.0 eV were attributed to S 2p_{3/2} and S 2p_{1/2} of S²⁻, respectively. The peaks at 164.6 and 168.0 eV were attributed to S₂²⁻ and the oxidation of sulfur species (S-SO₄²⁻) in CuS [40, 41]. Significantly, the peak of N 1s was observed only in CuS/MIL-Fe catalyst (Fig. S3b). N1s XPS spectrum showed two prominent peaks corresponding to the C-N bond and N-H group [42,43]. The FTIR and XPS analysis of CuS/MIL-Fe proved that the introduction of the -NH₂ group might change the morphology of MIL-101(Fe), which was

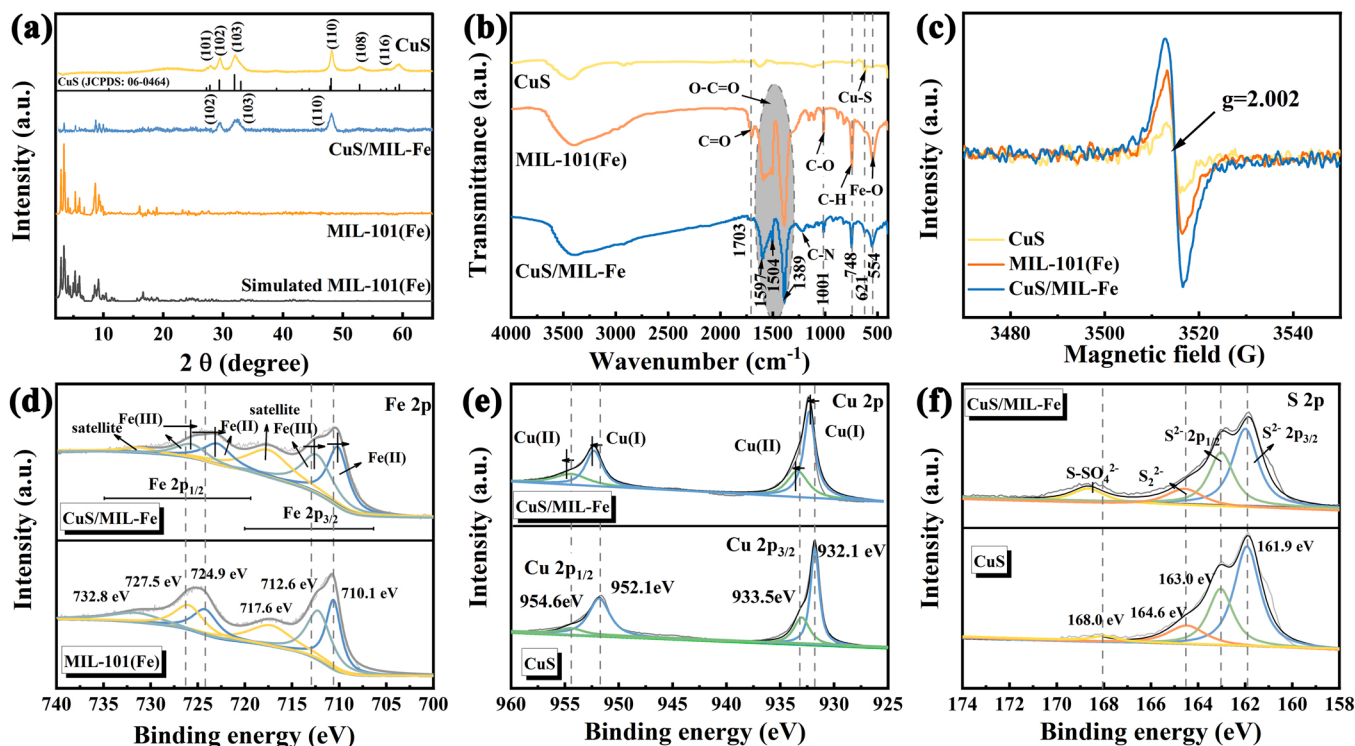


Fig. 2. (a) XRD, (b) FT-IR, (c) ESR spectra, and XPS spectra of (d) Fe 2p, (e) Cu 2p, and (f) S 2p of as-prepared catalysts.

consistent with the results discussed by Zhang et al. [25]. It was worth noting that the peaks of Fe 2p exhibited a negative shift while the peaks of Cu 2p and S 2p shift positively after coupling MIL-101(Fe) with CuS and constructing the heterojunction CuS/MIL-Fe (Figs. 2d and 2f), indicating that the electron cloud density of Fe increased while that of Cu and S decreased [38]. In summary, electrons transferred from CuS to MIL-101(Fe) in CuS/MIL-Fe interface.

Density functional theory (DFT) calculations were applied to further reveal the charge transfer path and the formation mechanism of CuS/MIL-Fe heterojunction in Fig. 3. Firstly, the work function (Φ) with applying to calculation of electrostatic potential in vertical direction of the monolayer was explored by the formula of $\Phi = V_{\infty} - E_f$. Here, V_{∞} is

the vacuum potential in the vicinity of selected material, and E_f is the Fermi energy level [44]. The computational results and values of CuS and MIL-101(Fe) in Fig. 3a and b show that the calculated work functions of CuS and MIL-101(Fe) were 5.43 and 5.92 eV versus vacuum level, respectively. The smaller work function of CuS tend to migrate electrons to MIL-101(Fe) through the interface of CuS and MIL-101(Fe). The result is directly proved by the charge density difference and planar-averaged electron density difference ($\Delta\rho$) in Fig. 3c. Distinctly, the charge redistribution occurs at the interface of CuS/MIL-Fe heterojunction. The results confirmed the electron transfer between CuS and MIL-101(Fe), and the trend of electron flow and accumulation on MIL-101(Fe) is observed, which was in good agreement with XPS

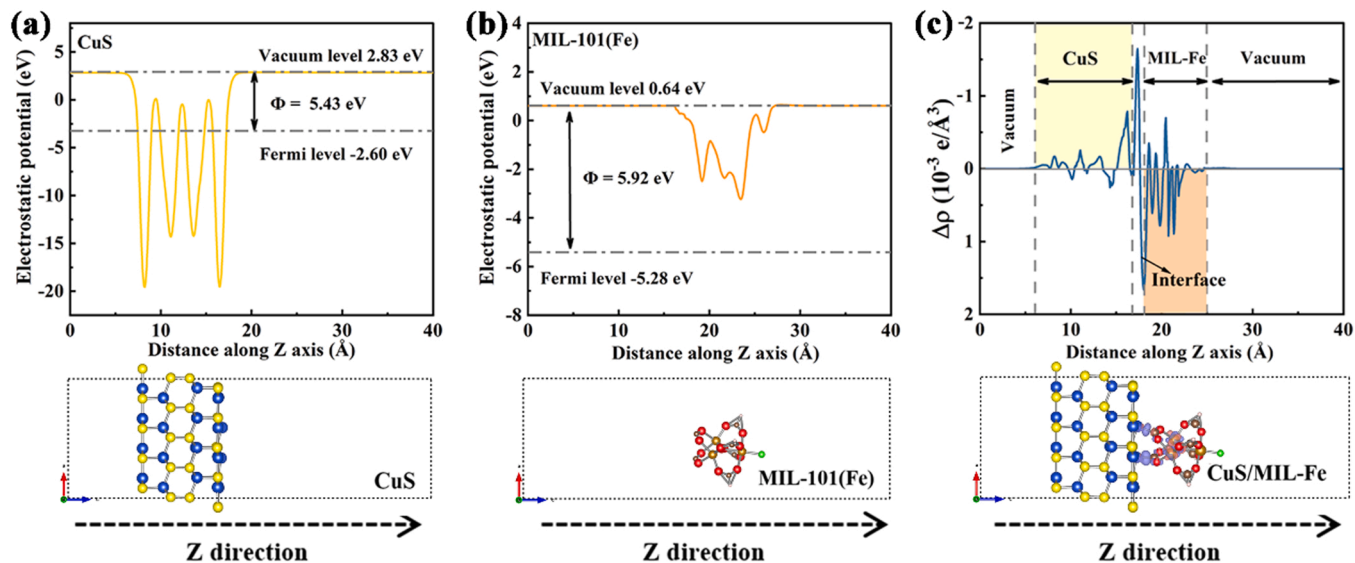


Fig. 3. The calculated work function and corresponding structural model of (a) CuS and (b) MIL-101(Fe); (c) the planar-averaged electron density difference and side view of the charge density difference over the CuS/MIL-Fe. The pink and purple regions of the construction represented the accumulation and depletion of electrons.

analysis. In addition, $\Delta\rho$ reveals the accumulation amount of electrons. The results showed that the CuS part near the interface displays positively charge, while the MIL-101(Fe) part near the interface is negatively charge due to the migration of electrons [45]. Thus, it could be concluded the heterojunction can be efficiently constructed by combining the CuS with MIL-101(Fe).

3.2. Photoelectrochemical test

Fig. 4a depicted the UV-vis diffuse reflectance spectra (DRS) of the as-prepared catalysts. MIL-101(Fe) possessed a high light absorption in the ultraviolet region of 200–650 nm. CuS showed a strong light response signal in the range of 200–800 nm due to the small band gap, and the recombination of CuS improved the light absorption capacity of MIL-101(Fe) [46]. In addition, the band gap energy of catalysts could be determined by Tauc curve which was calculated by following equation [47]:

$$\alpha(h\nu) = A(h\nu - E_g)^{1/2} \quad (1)$$

where α , ν , A , and E_g is the absorption coefficient, light frequency, a constant, and the band gap energy, respectively. Fig. 4b showed that the calculated E_g of CuS, MIL-101(Fe), CuS/MIL-Fe were 1.80, 2.71, and 2.18 eV, respectively. Fig. 4c indicated that the VB-XPS spectra could

infer that the approximate distance from valence band (VB) edge level to the Fermi level (E_f) of CuS, MIL-101(Fe) and CuS/MIL-Fe were 0.78, 1.99, and 1.22 eV, respectively. Then Mott-Schottky (M-S) plots measured the flat band potential of CuS, MIL-101(Fe), and CuS/MIL-Fe were at 0.18, -0.48 , and -0.29 V vs NHE (Fig. 4d), which indicated that MIL-101(Fe) and CuS were typical n-type and p-type semiconductors, respectively. The p - n heterojunction was formed after the combination of the two types of semiconductors. The flat band potential reflects the differences between E_f and water-reduction potential of as-prepared catalysts [48]. Thus, approximate VB level of as-prepared samples can be inferred. On the basis of the formula of $E_{CB} = E_{VB} - E_g$, the corresponding conduction band (CB) values of as-prepared samples were obtained. CuS and MIL-101(Fe) are typical p-type semiconductors and n-type semiconductors, respectively, in Fig. 4d. Due to the thermal balance of different E_f levels and the generation of the built-in electric field, VB and CB are rearranged, and the VB of CuS and CB level of MIL-101(Fe) are respectively close to E_f level to form p - n heterojunction [49], as shown in Fig. 4j. The VB of CuS and the CB of MIL-101(Fe) driven by the built-in electric field were rearranged to -1.51 and 0.67 V, respectively. The type II heterojunction might be formed between the two semiconductors. e^- generated in the CB of CuS would transfer to MIL-101(Fe), and h^+ produced by the VB of MIL-101(Fe) was migrated to CuS.

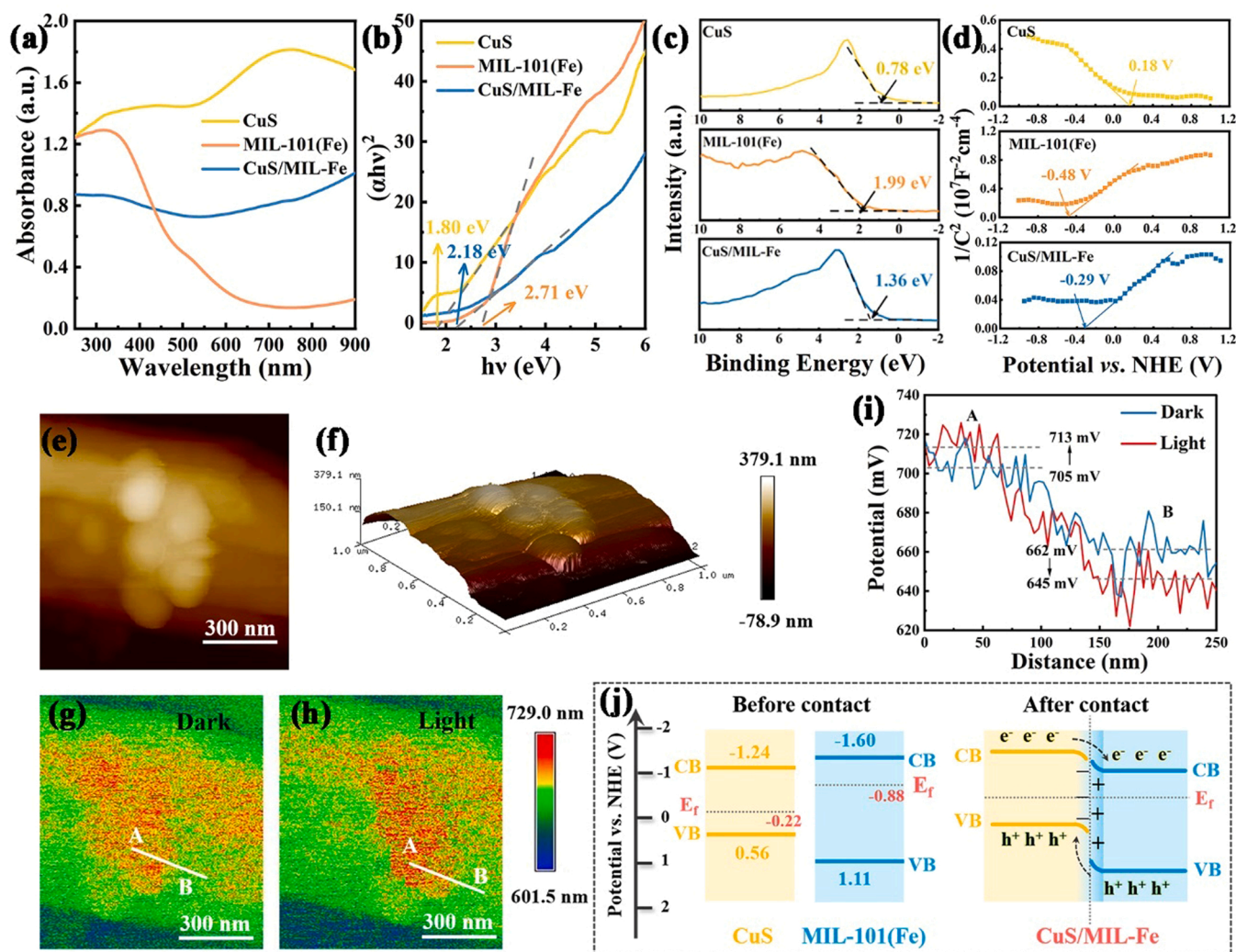


Fig. 4. (a) UV-vis DRS spectra. (b) Tauc plots. (c) VB-XPS spectra. (d) M-S plots. (e) 2D and (f) 3D atomic force microscopy image of CuS/MIL-Fe. Corresponding surface potential distribution of CuS/MIL-Fe (g) in darkness and (h) under light irradiation. (i) the line-scanning surface potential from point A to B. (j) Band structure diagrams.

In-situ Kelvin probe force microscopy (KPFM) was used to investigate built-in electric field in the interface between CuS and MIL-101(Fe). Fig. 4e and f showed that CuS appeared rugged on the surface of MIL-101(Fe). KPFM coupled with illumination enables directly visualizing of photoinduced charges separation and transfer direction in semiconductors [50]. Fig. 4g and h were the corresponding surface potential diagram before and under the light in which an illustrative line scan crossed the interface between CuS (A) and MIL-101(Fe) (B). Fig. 4i showed that the surface potential difference (SPD) of CuS/MIL-Fe heterojunction was estimated to be 43 mV in the dark and increased to 68 mV under the light. The SPD change of 25 mV was attributed to the generation of photoexcited carriers, which is the result of the enhancement of the electric interface field. In other words, this corresponded to the charge transfer mechanism of type II [51]. Meanwhile, the surface potential of A increased under the light while the surface potential of B decreased, which were attributed to the diffusion and accumulation of photoexcited electrons and holes on the n-MIL-101(Fe) and p-CuS sides

when illuminated [52], as shown in Fig. 4j. The result was in good agreement with DFT. Photoluminescence (PL) spectra were investigated the separation abilities of the photo-induced charge carriers in the as-prepared samples. As shown in Fig. S4a, compared with CuS and MIL-101(Fe) alone, the PL intensity of CuS/MIL-Fe decreased remarkably, indicating that heterojunction inhibited the recombination of electron and hole [53]. Fig. S4b exhibited that cyclic voltammetry (CV) curves of as-prepared catalysts, which indicated that the combination of CuS with MIL-101(Fe) could significantly improve the current density and redox capacity of the latter [54]. The photocurrent-time measurement was exploited to characterize the CuS, MIL-101(Fe) and CuS/MIL-Fe samples under dark and light. The result showed that the photoelectric response intensity of CuS/MIL-Fe was the highest (Fig. S4c). Overall, the MIL-101(Fe) modified with CuS increased the utilization of light energy, accelerated the transfer and separation of photon-generated carriers, and thus could improve the catalytic activity.

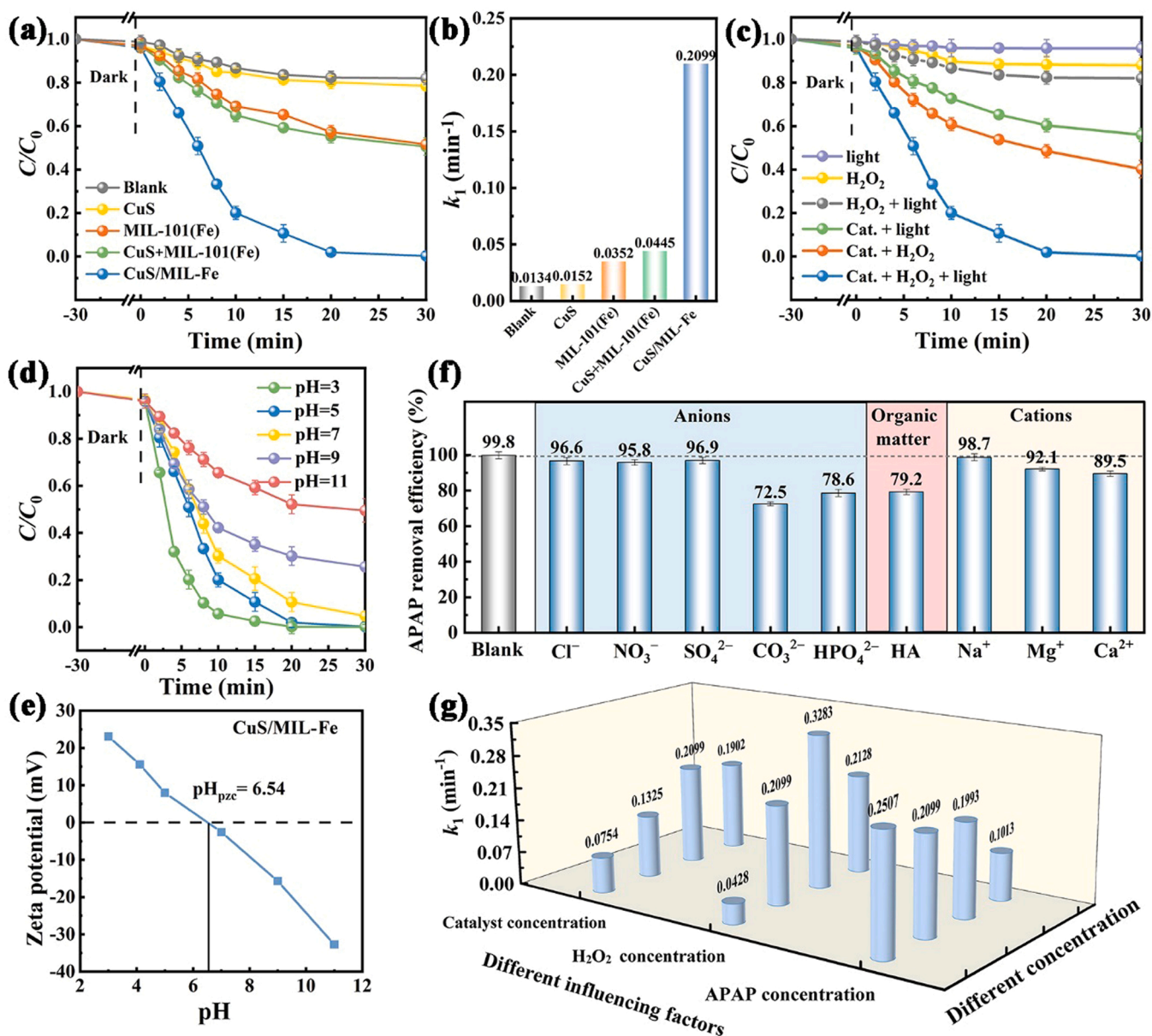


Fig. 5. (a) Photo-Fenton degradation of APAP; (b) rate constants by catalysts; (c) the effect of reaction system; (d) pH effects; (e) Zeta potentials of CuS/MIL-Fe dispersed into DI water at different pH values; (f) anions effect; (g) CuS/MIL-Fe concentration (50, 100, 200 and 300 mg·L⁻¹), H₂O₂ concentration (5, 15, 20, and 25 mM), and APAP concentration (2.5, 5, 7.5, and 10 mg·L⁻¹) on photo-Fenton degradation of CuS/MIL-Fe. Reaction condition: [catalyst] = 200 mg·L⁻¹, [30% H₂O₂] = 15 mM, [APAP] = 5 mg·L⁻¹, [anions] = 5 mM, and initial pH = 5 ± 0.2. The value of error bar stands for standard deviation (n = 3), the same below.

3.3. Photo-Fenton activities

3.3.1. Comparison of APAP degradation in different systems

The degradation of APAP in different systems was compared in Fig. 5a. "Blank" means only H_2O_2 without catalyst degraded APAP under light condition. After adding CuS alone, the removal efficiency of APAP was almost the same as blank, indicating that the decomposition of H_2O_2 by CuS was very weak and could be ignored. When CuS and MIL-101(Fe) were added at the same time, representing the physical mixture, the degradation efficiency of APAP was almost the same as MIL-101(Fe) alone. Surprisingly, the addition of CuS/MIL-Fe made the removal efficiency of APAP closed to 100%, which was significantly higher than all the above samples. In addition, the effect of the mass ratio of CuS to MIL-101(Fe) on the catalytic activity of CuS/MIL-Fe was also investigated (Fig. S5a), and the specific analysis was in Text S8. The 1:1 mass ratio of CuS to MIL-101(Fe) in the CuS/MIL-Fe composite exhibited the most excellent degradation performance, which was selected in this study. Fig. S5b showed that the photo-Fenton degradation of APAP by MIL-N was slightly higher than that of MIL-101(Fe), and the effect was not significantly improved. Therefore, we inferred that the substantial improvement of the degradation effect of CuS/MIL-Fe compared to MIL-101(Fe) was mainly due to the formation of heterojunction, and the influence of morphology, structure, and pore characteristics was insignificant. Fig. 5b showed that the pseudo-first-order rate constant (k_1) was also increased by more than 5 times than MIL-101(Fe) and CuS + MIL-101(Fe) systems. The results indicated that there was chemical attraction between CuS and MIL-101(Fe) to form heterojunction which could inhibit electron hole recombination. Meanwhile, the redox process of Fe ions was accelerated to promote the decomposition of H_2O_2 .

Furthermore, the effect of light and H_2O_2 on the catalytic activity was verified in Fig. 5c. Either individual H_2O_2 or light showed negligible degradation of APAP, while the combination of H_2O_2 and light exhibited certain removal capacity on APAP due to the activation of H_2O_2 by the light irradiation. In the presence of light or H_2O_2 alone, CuS/MIL-Fe had a certain degradation efficiency on APAP degradation of 44.1 % and 59.8 %, respectively. Even in the absence of H_2O_2 , CuS/MIL-Fe as a photocatalyst could induce APAP degradation. Under dark conditions, CuS/MIL-Fe could decompose H_2O_2 to produce ROS to promote APAP removal, and the degradation of APAP is primarily based on Fenton reaction. These results indicated that, on the one hand, CuS/MIL-Fe heterojunction could reduce the recombination of electron-hole pairs and produce unique and highly oxidizing substances (h^+) in photo-degradation. On the other hand, CuS can accelerate the regeneration of Fe (II) as the active site and promote the decomposition of H_2O_2 in Fenton degradation. In the photo-Fenton system, CuS/MIL-Fe catalyst constructed a high-speed electron transfer channel as a bridge to transfer the photo-generated electrons, which could accelerate the valence state transition of Fe to promote the decomposition of H_2O_2 . Moreover, compared with the literature data as shown in Table S1, the CuS/MIL-Fe exhibited excellent catalysis activity to degrade APAP in the photo-Fenton system.

3.3.2. Effect of pH value

As illustrated in Fig. 5d, the effect of initial pH between 3.0 and 11.0 on APAP removal efficiency was studied. Under the condition of pH from acidic to neutral, the removal efficiency of APAP could reach more than 95%, and the degradation rate was faster at lower pH. The change of pH during the reaction was monitored, indicating that pH decreased slightly along with the degradation of APAP (Fig. S5c). It might be due to the production of H^+ ($\text{S}^{2-} + 8\text{Fe(III)}/\text{Cu(II)} + 4\text{H}_2\text{O} \rightarrow 8\text{Fe(II)}/\text{Cu(I)} + \text{SO}_4^{2-} + 8\text{H}^+$) [55]. Acidic condition could promote the decomposition of H_2O_2 to produce more ROS such as $\bullet\text{OH}$ [56]. Meanwhile, the stability of H_2O_2 was better under acidic condition than other condition [57]. Therefore, CuS/MIL-Fe had a better performance under acidic condition. Fig. 5e showed the zeta potentials of CuS/MIL-Fe dispersed into water under different pH. CuS/MIL-Fe was negatively charged in

the alkaline condition. The pKa of APAP is 9.38 (Fig. S5d), thus strong alkaline conditions might trigger the deprotonation of APAP [58]. Therefore, the mutual repulsion between the CuS/MIL-Fe catalyst and the deprotonated APAP might prevent them from contacting under the alkaline conditions. The removal efficiency of APAP was significantly reduced in alkaline system.

3.3.3. Effect of anions, NOM, and cations

Fig. 5f exhibited the effect of anions (Cl^- , NO_3^- , SO_4^{2-} , CO_3^{2-} , and H_2PO_4^-), natural organic matter (NOM), and cations (Na^+ , Mg^{2+} , and Ca^{2+}) on the removal efficiency of APAP, respectively. After the addition of Cl^- , NO_3^- , and SO_4^{2-} , the removal efficiency of APAP could still reach more than 95%, indicating that these three anions have hardly effects on the photo-Fenton reaction. Due to the increase in pH value caused by CO_3^{2-} , the removal efficiency dropped from 99.8% to 72.5% after the addition of CO_3^{2-} , which was consistent with the effect of pH value on APAP degradation in Fig. 5d. Meanwhile, it might be due to the quenching effect of CO_3^{2-} on $\bullet\text{OH}$ radicals to form less-reactive $\text{CO}_3^{\bullet-}$ radicals [59]. Moreover, the removal efficiency also significantly decreased from 99.8% to 72.5% after adding H_2PO_4^- , which might be due to the occupation of portion active sites on CuS/MIL-Fe by H_2PO_4^- , which was not conducive to APAP degradation [59]. Meanwhile, H_2PO_4^- was effective in scavenging $\bullet\text{OH}$ radicals to produce $\text{H}_2\text{PO}_4^{\bullet}$ radicals with weaker oxidation capacity [60]. Humic acid (HA) is a typical natural organic compound. It casted a certain inhibitory effect on the degradation of APAP, which was attributed to the competition between HA and hydrogen peroxide for active sites. Meanwhile, HA might scavenge the free radicals and photo-generated holes [61], thus prohibiting the degradation reaction. The cations could also slightly inhibit the degradation reaction, and the inhibition effect followed the order: $\text{Ca}^{2+} > \text{Mg}^{2+} > \text{Na}^+$. It was due to the fact that the cations might compete with Fe(II) to occupy the active sites on the catalyst and the high ionic strength would lead to catalyst agglomeration [28]. The negligible inhibition effect of Na^+ was owned to its low piezoelectric bilayer effect and weak ion exchange capacity [62]. Taken together, CuS/MIL-Fe had practical feasibility in sewage remediation.

3.3.4. Effect of CuS/MIL-Fe, H_2O_2 , and APAP concentration

The effect of catalyst, H_2O_2 and APAP concentration on photo-Fenton degradation of APAP in CuS/MIL-Fe system was explored. The removal efficiencies of APAP and the corresponding k_1 under different conditions were shown in Fig. S6 and Fig. 5g, respectively. The results showed that k_1 increased and then decreased with the increase of catalyst concentration. The appropriate amount of catalysts could increase the reaction site and photo-generated e^- and h^+ . However, when the catalyst concentration was excessive, it would increase the turbidity in the reactor and reduce the light transmittance [63]. When the concentration of H_2O_2 increased to 20 mM, the degradation rate of APAP could reach 0.3283 min^{-1} , and then decreased significantly as the concentration of H_2O_2 continued to increase. This could be attributed to the fact that appropriate H_2O_2 could accelerate the photo-Fenton reaction, and excess H_2O_2 could capture free radicals [6]. Moreover, with the increase of APAP concentration from 2.5 to $10\text{ mg}\cdot\text{L}^{-1}$, the k_1 decreased from 0.2507 to 0.1013 min^{-1} . APAP was hardly adsorbed by CuS/MIL-Fe confirmed by adsorption experiments, indicating that APAP mainly existed in the liquid phase. With the increase in APAP concentration, the amount of reactive oxygen species (ROS) in the reaction system was insufficient, so excessive APAP in the liquid phase could be hardly degraded [64,65].

3.4. Optimization of the APAP degradation by CuS/MIL-Fe

The central composite design (CCD) based on response surface methodology using Design Expert 12 software was employed to optimize the photo-Fenton degradation conditions of APAP, including catalyst concentration (A), H_2O_2 concentration (B), and initial pH (C), and the

removal efficiency of APAP (Y) was the response variable. The range of independent variables set according to the preliminary experiment was shown in Table S2. The experimental design of CCD and results including experimental and predicted values are shown in Table S3. The above data was fitted by multiple regression to obtain the quadratic polynomial regression equation between the independent variable and the dependent variable:

$$Y = 98.14 + 3.66 A + 7.08 B - 7.55 C + 3.81 AB + 5.32 AC - 2.25 BCE - 10.02 A^2 - 14.27 B^2 - 5.62 C^2 \quad (2)$$

These plus-minus coefficients determined the positive and negative effects between the independent variables and the surface response. The normal probability plots of residuals and the plot of residuals vs. Run verified the adequacy of the model (Fig. S7). The reliability of the model is proved by the response relationship between the residual value and the predicted value. Meanwhile, the correlation and significance of the proposed model were verified by analysis of variance (ANOVA) based on

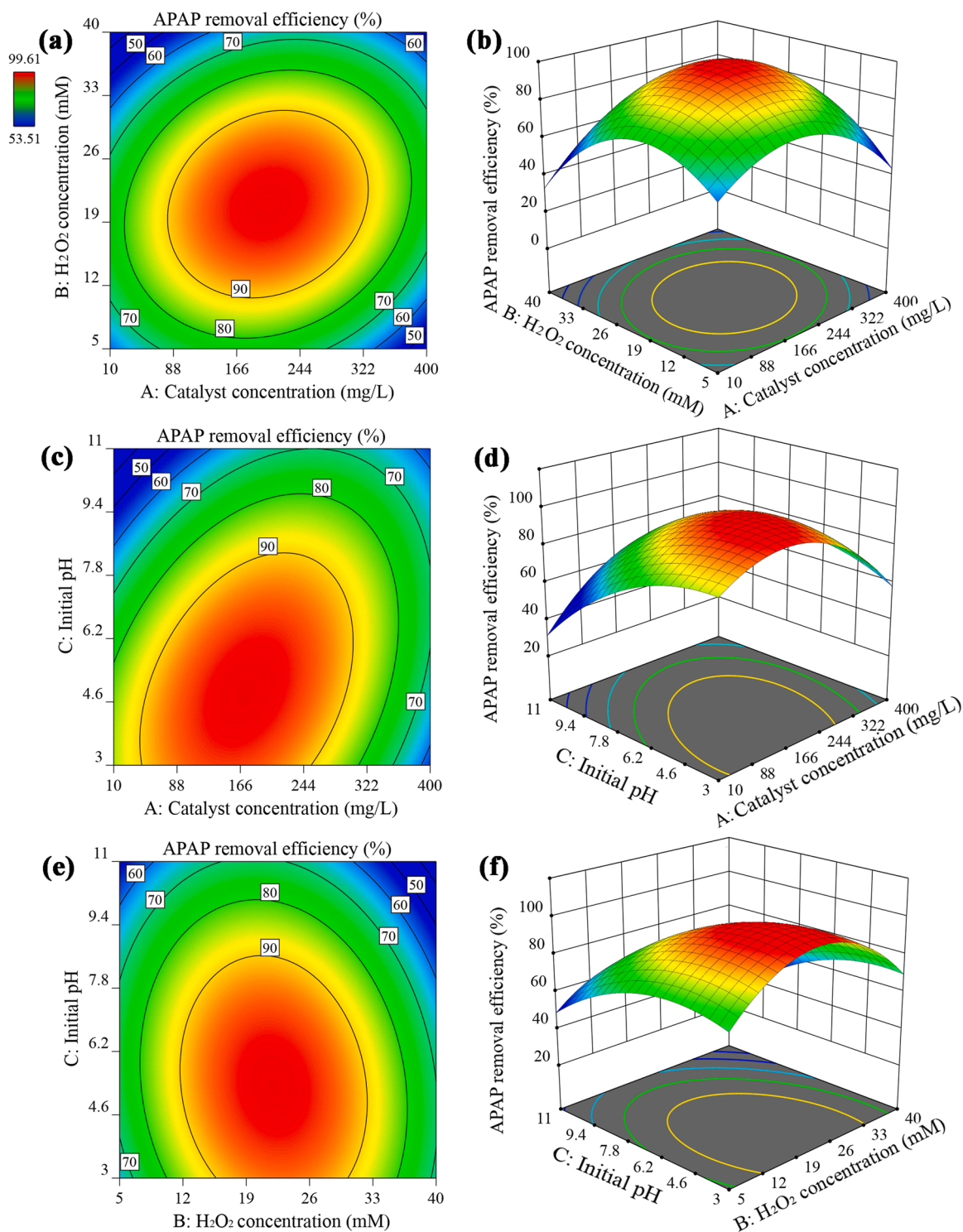


Fig. 6. 2D contour and 3D surface plots as a function of (a, b) catalyst and H₂O₂ concentration, (c, d) catalyst concentration and pH, and (e, f) H₂O₂ concentration and pH on the removal efficiency of APAP.

Fisher's test (F-test) [66]. The detailed description and judgment method were in Text S9 and Table S4. The results show that the proposed model has high accuracy and reliability, and can effectively describe the relationship between APAP removal efficiency and independent variables.

The two-dimensional (2D) contour and three-dimensional (3D) response surface plots displayed the interaction between APAP removal efficiency and two independent variables (AB, AC, BC). The shape of the 2D contour diagram included circle and ellipse, and the ellipse contour reflected significant interaction. Fig. 6a and b showed that the degradation efficiency of APAP gradually reached the best and then began decrease with the increase of H_2O_2 concentration and catalyst concentration at initial pH of 6.5. Excessive H_2O_2 and CuS/MIL-Fe could inhibit the reaction, the detailed reasons were detailed in 3.3.4. Fig. 6c and d displayed that the removal efficiency of APAP gradually increased with the gradual increase of pH and catalyst dosage under the condition of H_2O_2 concentration of 17.5 mM. With the further increase of catalyst dosage, the APAP removal efficiency would have a negative impact, and the APAP removal efficiency reached the highest in acidic pH region. The trend of Fig. 6e and f was similar to Fig. 6c and d under the condition of catalyst concentration of $175 \text{ mg}\cdot\text{L}^{-1}$. When selecting the initial pH and hydrogen peroxide concentration, the catalyst concentration at $100\text{--}300 \text{ mg}\cdot\text{L}^{-1}$ has no significant influence on the optimal degradation efficiency. In summary, based on response surface analysis, the range of optimal reaction conditions was simulated: the CuS/MIL-Fe concentration ($100\text{--}300 \text{ mg}\cdot\text{L}^{-1}$), the H_2O_2 concentration ($13\text{--}30 \text{ mM}$), and the initial pH ($3\text{--}7$), and removal efficiency of APAP could reach more than 90%. In addition, verification experiments were carried out within the range of optimal conditions. When the catalyst concentration was $200 \text{ mg}\cdot\text{L}^{-1}$, the H_2O_2 concentration was 15 mM and the initial pH was 5, removal efficiency of APAP obtained was 99.8%, which was basically consistent with the predicted value (99.99%). The results showed that the model was reliable and could predict the optimal operating conditions well of APAP degradation.

3.5. Reusability and stability of CuS/MIL-Fe

The recyclability of the catalyst is a significant index of industrial application, so five cycling experiments are used to inspect the stability of the CuS/MIL-Fe. The efficiency degradation of APAP still maintains 89.9% after 5 cycles (Fig. 7a). This might be due to the leaching of metals, which reduced the number of active sites. The stability of CuS/MIL-Fe under the pH from 3.0 to 11.0 was investigated in Figs. S8 and S9. The specific description was in Text S10. However, the leaching concentrations of Cu and Fe were 0.35 and $0.14 \text{ mg}\cdot\text{L}^{-1}$ based on the ICP measurement, respectively, which are far below the emission standard [63]. Fig. S10 showed that the removal efficiency of APAP in the homogeneous system was 35.6 %, indicating that heterogeneous catalysis played a leading role in the photo-Fenton degradation APAP system [61]. S^{2-} could be released from CuS/MIL-Fe under acidic condition and S^{2-} has trifling effect on photo-Fenton degradation of APAP, which was detailed in Text S11. In addition, Fig. 7b was conducted to investigate the crystallinity of fresh and used CuS/MIL-Fe. The results of XRD patterns remained basically unchanged. Fig. S11 showed that the ESR signal intensity of used catalyst decreases slightly compared with the fresh catalyst, indicating that most defects remain after the reaction. Fig. 7c showed that the intensity of Cu 2p and S 2p were declined, which was attributed to loss of Cu and oxidation of S. Fig. 7d displayed that the Fe 2p performs a little difference in binding energy, and about 3.5% of Fe (II) was converted to Fe(III), which proved that the addition of CuS ensured the circulation of Fe(II)/Fe(III). In Fig. 7e, the satellite peaks at 943.2 and 963.0 eV were also observed, corresponding to the increase in the relative intensity ratio of Cu(I) [67]. Fig. 7f showed that the proportion of S^{2-} decreases from 75.0 % to 59.6 %, $\text{S}\text{-SO}_4^{2-}$ increases from 10.3 % to 22.6 %, and the S_2^{2-} is basically unchanged. The result suggests that S^{2-} and Cu(I) acts as an electron donor to realize Fe(II)/Fe(III) redox cycle, which accelerates the decomposition process of H_2O_2 and further promotes APAP degradation.

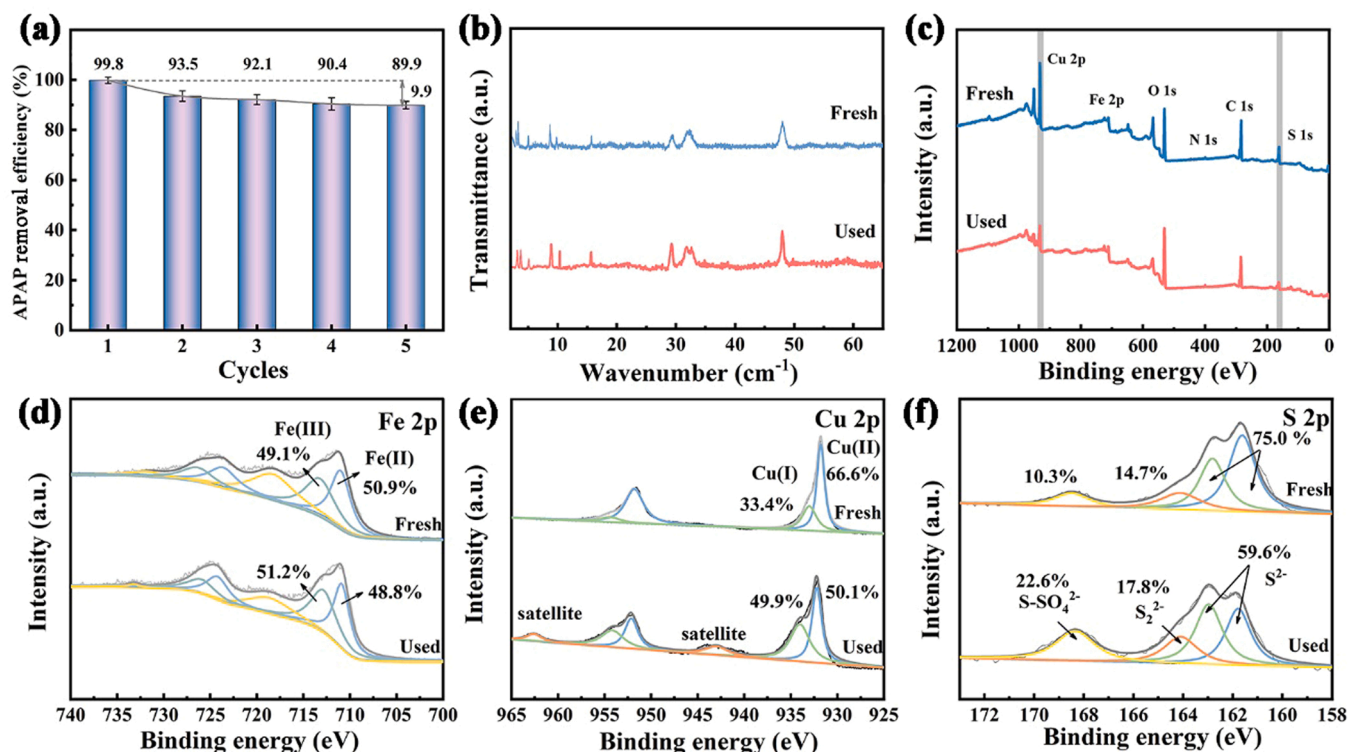


Fig. 7. (a) Five cycling experiments. Reaction condition: [catalyst] = $200 \text{ mg}\cdot\text{L}^{-1}$, $[\text{30}\% \text{H}_2\text{O}_2]$ = 15 mM , [APAP] = $5 \text{ mg}\cdot\text{L}^{-1}$, and initial pH = 5 ± 0.2 . (b) XRD pattern and XPS spectra of (c) survey scan, (d) Fe 2p; and (e) Cu 2p; and (f) S 2p of fresh and used CuS/MIL-Fe.

3.6. Photo-Fenton degradation mechanism

To explore the synergy between the decomposition of H_2O_2 and light irradiation in the CuS/MIL-Fe system, ROS during the photo-Fenton reaction was determined through the classical quenching tests. Several types of scavengers, benzoquinone (BQ), EDTA-2Na, tert-butyl alcohol (TBA), AgNO_3 and L-histidine, were added to act as quenching agents for the scavenging of $\bullet\text{O}_2^-$, h^+ , $\bullet\text{OH}$, e^- and $^1\text{O}_2$, respectively. Figs. S12, 8a, and 8b showed the removal efficiency of APAP the k_1 in the presence of different quenching agents under different systems. Fig. 8a showed that $\bullet\text{O}_2^-$ has a slight effect, and h^+ , $\bullet\text{OH}$, e^- and $^1\text{O}_2$ have a certain promotion effect on the photo-Fenton degradation. For the Fenton degradation (Fig. 8b), the main active substance was $\bullet\text{OH}$, and part of $\bullet\text{OH}$ might convert into $^1\text{O}_2$ and $\bullet\text{O}_2^-$ to participate in the degradation reaction [40]. For the photo degradation, the strong oxidizing h^+ and $\bullet\text{O}_2^-$ played a major role, in which part of $\bullet\text{O}_2^-$ was converted into $^1\text{O}_2$, and it was found that no $\bullet\text{OH}$ was generated. As shown in Fig. 4j, the photo-generated e^- could react with O_2 to generate $\bullet\text{O}_2^-$ because the CB potential of MIL-101(Fe) (-1.57 V) was more negative than that of $\text{O}_2/\bullet\text{O}_2^-$ (-0.33 V). However, the photo-generated h^+ of CuS could not generate $\bullet\text{OH}$, because the VB position of CuS (0.67 V) was not higher than the redox potential of $\text{OH}^-/\bullet\text{OH}$ (1.99 V) [49]. Therefore, CuS/MIL-Fe acted as a photocatalyst to form the type II heterojunction, which is consistent with the results of photoelectrochemical test. The k_1 values of the quenching experiment were used to estimate the contribution of different ROS in the degradation process (Fig. 8c) [58]. The results showed that the inhibition rate of $^1\text{O}_2$ and e^- in photo-Fenton reaction was significantly higher than that in Fenton reaction and photodegradation, respectively. CuS/MIL-Fe with the structure of p-n heterojunction not only increased the new ROS (h^+) to convert low oxidation capacity $\bullet\text{O}_2^-$ to $^1\text{O}_2$, but also successfully established an efficient electron transfer channel between photodegradation and Fenton degradation to accelerate the redox of active sites in Fenton reaction. Fig. 8d showed that light radiation could accelerate the decomposition

of H_2O_2 .

ESR spin-trap technology was carried out by using DMPO and TEMP as the radical scavenger to further verify the above conclusions (Fig. 8e). The results showed that the four characteristic peaks of DMPO- $\bullet\text{OH}$ are only produced when H_2O_2 was added, which is consistent with the previous quenching experimental results. The signal intensity of CuS/MIL-Fe/ H_2O_2 system increased significantly after the light radiation, indicated that more $\bullet\text{OH}$ could be generated under light radiation. Fig. S13 showed that the DMPO- $\bullet\text{OH}$ signal of H_2O_2 alone system was far below that of CuS/MIL-Fe/ H_2O_2 system under light radiation, indicating that a small amount of H_2O_2 would decompose into $\bullet\text{OH}$ under light radiation. Meanwhile, there was no signal of TEMP- $^1\text{O}_2$ and DMPO- $\bullet\text{O}_2^-$ in H_2O_2 /light system, implying that the presence of CuS/MIL-Fe heterojunction might construct electron transfer channel, and thus promoting the formation of ROS. TEMP- $^1\text{O}_2$ was observed in all three systems, but the $^1\text{O}_2$ signal intensity in the photo-Fenton system was much stronger than the other two systems. The signal intensity of DMPO- $\bullet\text{O}_2^-$ remained almost unchanged in the three systems, indicating that $\bullet\text{O}_2^-$ radicals were not the main ROS that caused the increase in APAP removal efficiency. Therefore, light irradiation could improve the ability of CuS/MIL-Fe to produce $^1\text{O}_2$ and $\bullet\text{OH}$ in the APAP degradation process.

The proposed photo-Fenton mechanism in the CuS/MIL-Fe system was present in Fig. 9. Firstly, CuS/MIL-Fe acted as a photocatalyst to generate electron and hole (e^- - h^+) pairs under simulating solar radiation (Eq. 3). Adsorbed oxygen decomposes into $\bullet\text{O}_2^-$ after obtaining electrons, h^+ could directly degrade APAP and promote $\bullet\text{O}_2^-$ to produce $^1\text{O}_2$ (Eqs. 4 and 5) [68]. Secondly, CuS/MIL-Fe as a Fenton reaction catalyst decomposed H_2O_2 into $\bullet\text{OH}$ through the electron cycle between Cu, Fe and S, further producing $\bullet\text{O}_2^-$ and $^1\text{O}_2$ (Eqs. 6–11) [38,69]. Therefore, the photo-generated e^- could promote the redox reactions of Fe and Cu through the electron transfer channel in photo-Fenton reaction. Meanwhile, light could also directly decompose H_2O_2 to generate $\bullet\text{OH}$ (Eq. 12) [70]. The reaction steps were listed in the following

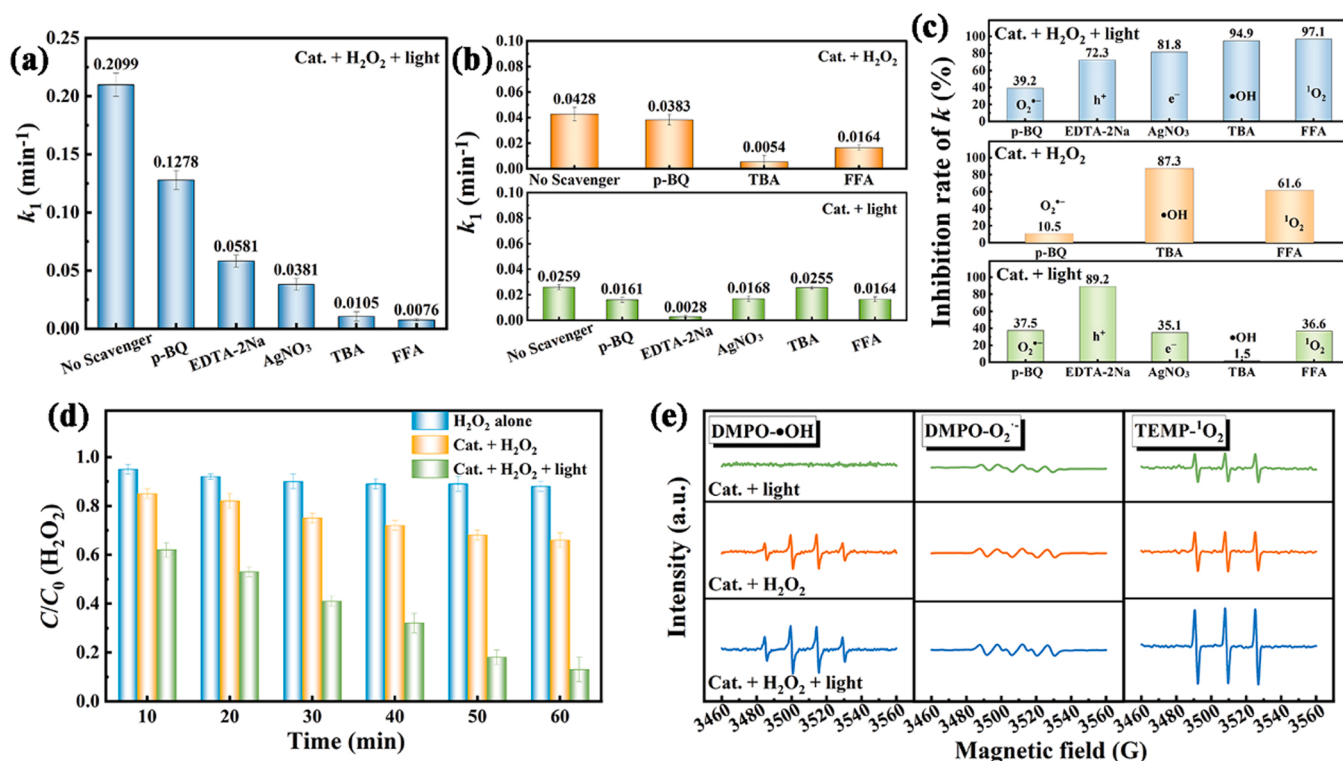


Fig. 8. The rate constants of (a) photo-Fenton degradation and (b) Fenton and photo degradation with different scavengers. Reaction condition: [catalyst] = $200\text{ mg}\cdot\text{L}^{-1}$, [30% H_2O_2] = 15 mM , [APAP] = $5\text{ mg}\cdot\text{L}^{-1}$, [TBA] = 200 mM , [AgNO_3] = 100 mM , [EDTA-2Na] = [FFA] = [p-BQ] = 10 mM , and initial pH = 5 ± 0.2 . (c) Inhibition rate of ROS. (d) The decomposition efficiency of H_2O_2 . (e) ESR spectra.

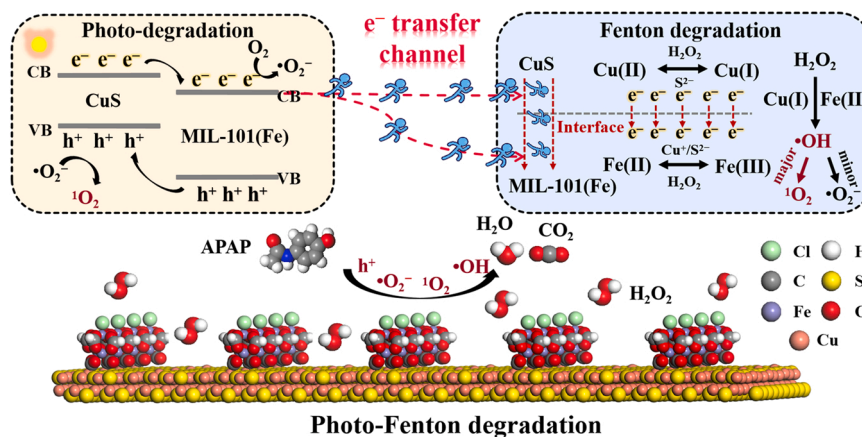


Fig. 9. Schematic illustration for the possible photo-Fenton degradation mechanism.

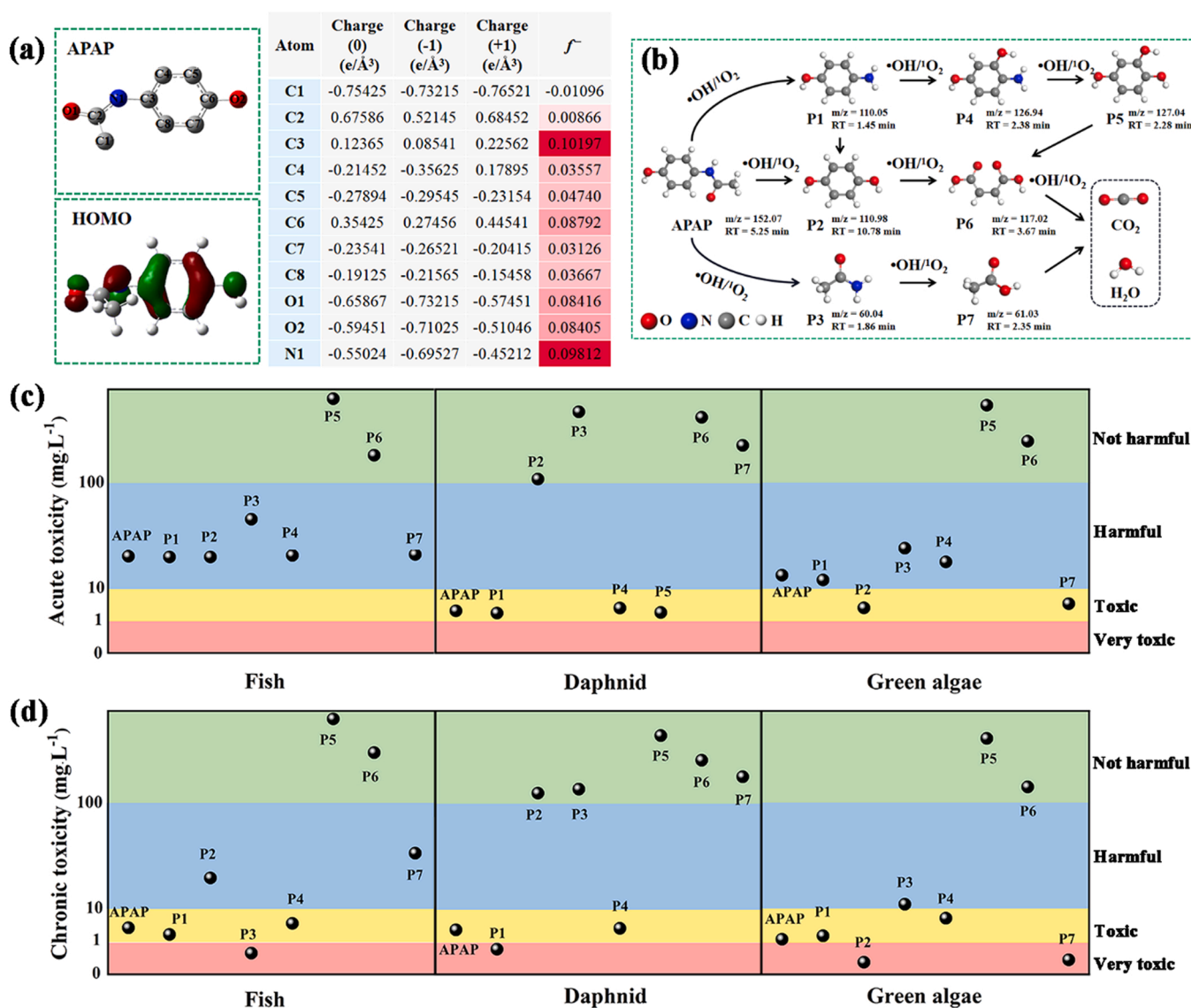
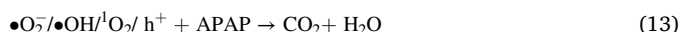
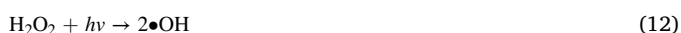
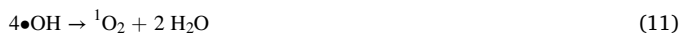
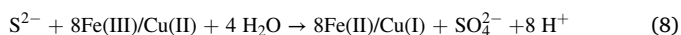
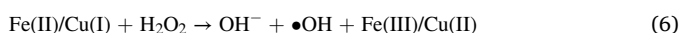
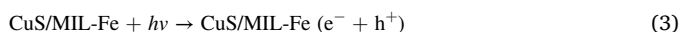


Fig. 10. (a) Possible pathways of APAP degradation. (b) The acute toxicity and (c) the chronic toxicity of APAP and intermediates for fish, daphnia, and green algae.

equations:



3.7. Possible degradation pathway and toxicity assessment of intermediate products

The Fukui index using Multiwfn software based on DFT revealed the most vulnerable sites of APAP by ROS attack [71]. $\bullet\text{OH}$ and ${}^1\text{O}_2$, as electrophilic ROS, would attack the electron losing sites in APAP molecules. Fig. 10a showed that the HOMO of APAP is mainly located on the benzene ring, C-O, N-C, and C=O bond. In order to show the reactivity of each atom more clearly, the natural population analysis (NPA) charge distribution and Fukui index (f^-) are listed in the Fig. 10a. The atom with the higher f^- value were easier to be attacked by $\bullet\text{OH}$ and ${}^1\text{O}_2$. Therefore, C3, C6, O1, O2, and N1 were also possible reactive sites for electrophiles [72]. However, C6, O1, and O2 were saturated already and could not further accept $\bullet\text{OH}$ and ${}^1\text{O}_2$ addition, thus C3 and N1 would be the overall possible sites for $\bullet\text{OH}$ and ${}^1\text{O}_2$. LC-MS measurement determines the possible seven intermediate products (Fig. S14 and Table S5), and the degradation pathway of APAP was deduced combined with Fukui index (Fig. 10b). Some acetamido in APAP would be attacked by $\bullet\text{OH}$ and ${}^1\text{O}_2$ which was matched with higher Fukui index of C3 (0.10197) and N1 (0.09812), and the C-N bond broke to generate P1 ($m/z = 110.05$) and P3 ($m/z = 60.04$). The generation of P4 ($m/z = 126.94$) was based on the hydroxyl addition. The amino groups in P1 and P4 might be attacked by $\bullet\text{OH}$ and ${}^1\text{O}_2$ to generate P2 ($m/z = 110.98$) and P5 ($m/z = 127.04$), and the benzene ring was further cleavage to generate P6 ($m/z = 117.02$), and the amino group in P3 was attacked to generate P7 ($m/z = 61.03$). P6 and P7 eventually turned into CO_2 and H_2O . Meanwhile, ecological structure activity relationship (ECOSAR) program was used to predict the acute and chronic toxicity of APAP and its intermediate products by quantitative structure-activity relationship (QSAR) analysis (Fig. 10c and d), which was detailed in Text S12. The results revealed that the acute toxicities of intermediate products were obviously reduced. In terms of the chronic toxicity, most intermediates showed lower toxicity to fish, daphnid, and green algae than APAP. However, some intermediates (P1, P2, P3, and P7) showed more toxic to them than APAP, indicating that the potential risks caused by some intermediate products of APAP needed to be concerned during the removal process. Moreover, CuS/MIL-Fe achieved a TOC removal rate of 60.12 % within 120 min (Fig. S15). Thus, this proposed technology is an efficient way for the mineralization of degraded intermediates [73].

4. Conclusion

In this work, a self-assembled CuS/MIL-Fe heterojunction was

designed to apply for efficient degradation of APAP via photo-Fenton reaction. The charge transfer pathway of heterojunction was identified by XPS analysis and DFT calculation, which provided the evidence of electron transfer from CuS to MIL-101(Fe) at the heterointerface. Besides, photo-irradiated KPFM measurement indicated that photo-generated electrons can be easily transported through the CuS/MIL-Fe interface. The close contact interface and high charge transfer conductivity realized the synergistic effect of photo and Fenton degradation by establishing a high-speed electron transfer channel. As expected, CuS/MIL-Fe showed superior activity for the photo-Fenton degradation of APAP, and the removal efficiency was close to 100% within 30 min under simulated sunlight. Overall, this study will open up a new insight into the application of heterojunction photo-Fenton technology in environmental remediation.

CRediT authorship contribution statement

Zhimo Fang: Conceptualization, Methodology, Software, Visualization, Investigation, Writing – original draft. **Yibo Liu:** Validation, Data curation. **Juanjuan Qi:** Writing – review & editing, Funding acquisition. **Zhongfei Xu:** Software. **Tieyue Qi:** Writing – review & editing. **Lidong Wang:** Writing – review & editing, Funding acquisition.

Declaration of Competing Interest

The authors declare that they have no known competing financial interests or personal relationships that could have appeared to influence the work reported in this paper.

Data Availability

Data will be made available on request.

Acknowledgments

This work was financially supported by the National Natural Science Foundation of China (No. 51878273, No. 22106045), the Natural Science Foundation of Hebei Province, China (No. E2019502199), and the Fundamental Research Funds for the Central Universities, China (No. 2021MS038). The authors would like to thank ECOSAR software supplied by the U.S. Environmental Protection Agency.

Appendix A. Supporting information

Supplementary data associated with this article can be found in the online version at doi:10.1016/j.apcatb.2022.121979.

References

- [1] C.I. Kosma, D.A. Lambropoulou, T.A. Albanis, Investigation of PPCPs in wastewater treatment plants in Greece: occurrence, removal and environmental risk assessment, *Sci. Total Environ.* 466–467 (2014) 421–438.
- [2] I.M. Sebastine, R.J. Wakeman, Consumption and environmental hazards of pharmaceutical substances in the UK, *Process Saf. Environ. Prot.* 81 (2003) 229–235.
- [3] M. Day, Covid-19: ibuprofen should not be used for managing symptoms, say doctors and scientists, *BMJ* 368 (2020) m1086.
- [4] Y. Li, Y. Pan, L. Lian, S. Yan, W. Song, X. Yang, Photosensitized degradation of acetaminophen in natural organic matter solutions: The role of triplet states and oxygen, *Water Res.* 109 (2017) 266–273.
- [5] Y. Qin, G. Li, L. Zhang, T. An, Protocatechuic acid promoted catalytic degradation of rhodamine B with Fe@Fe₂O₃ core-shell nanowires by molecular oxygen activation mechanism, *Catal. Today* 335 (2019) 144–150.
- [6] Y. Qin, L. Zhang, T. An, Hydrothermal carbon-mediated fenton-like reaction mechanism in the degradation of alachlor: direct electron transfer from hydrothermal carbon to Fe(III), *ACS Appl. Mater. Interfaces* 9 (2017) 17115–17124.
- [7] M. Qian, L. Yang, X. Chen, K. Li, W. Xue, Y. Li, H. Zhao, G. Cao, X. Guan, G. Shen, The treatment of veterinary antibiotics in swine wastewater by biodegradation and Fenton-like oxidation, *Sci. Total. Environ.* 710 (2020), 136299.

- [8] L. Wang, P. Jin, S. Duan, J. Huang, H. She, Q. Wang, T. An, Accelerated Fenton-like kinetics by visible-light-driven catalysis over iron(III) porphyrin functionalized zirconium MOF: effective promotion on the degradation of organic contaminants, *Environ. Sci.: Nano* 6 (2019) 2652–2661.
- [9] F.-X. Wang, C.-C. Wang, X. Du, Y. Li, F. Wang, P. Wang, Efficient removal of emerging organic contaminants via photo-Fenton process over micron-sized Fe-MOF sheet, *Chem. Eng. J.* 429 (2022), 132495.
- [10] X. Qian, M. Ren, Y. Zhu, D. Yue, Y. Han, J. Jia, Y. Zhao, Visible light assisted heterogeneous fenton-like degradation of organic pollutant via α -FeOOH/mesoporous carbon composites, *Environ. Sci. Technol.* 51 (2017) 3993–4000.
- [11] Q. Zhao, C.-C. Wang, P. Wang, Effective norfloxacin elimination via photo-Fenton process over the MIL-101(Fe)-NH₂ immobilized on α -Al₂O₃ shee, *Chin. Chem. Lett.*, <https://doi.org/10.1016/j.cclet.2022.1001.1033>.
- [12] T. Wang, C. Nie, Z. Ao, S. Wang, T. An, Recent progress in g-C₃N₄ quantum dots: synthesis, properties and applications in photocatalytic degradation of organic pollutants, *J. Mater. Chem. A* 8 (2020) 485–502.
- [13] H. Liu, X. Chang, X. Liu, G. Li, W. Zhang, T. An, Boosting the photocatalytic degradation of ethyl acetate by a Z-scheme Au-TiO₂@NH₂-UiO-66 heterojunction with ultrafine Au as an electron mediator, *Environ. Sci.: Nano* 8 (2021) 2542–2553.
- [14] C.-Y. Wang, L. Ma, C.-C. Wang, P. Wang, L. Gutierrez, W. Zheng, Light-response adsorption and desorption behaviors of metal-organic frameworks, *Environ. Funct. Mater.* 1 (2022) 49–66.
- [15] Q. Zhao, X.-H. Yi, C.-C. Wang, P. Wang, W. Zheng, Photocatalytic Cr(VI) reduction over MIL-101(Fe)-NH₂ immobilized on alumina substrate: From batch test to continuous operation, *Chem. Eng. J.* 429 (2022), 132497.
- [16] H. Liu, N. Li, M. Feng, G. Li, W. Zhang, T. An, Near-infrared light induced adsorption-desorption cycle for VOC recovery by integration of metal-organic frameworks with graphene oxide nanosheets, *Environ. Sci.: Nano* 9 (2022) 1858–1868.
- [17] F. Zhao, Y. Liu, S.B. Hammouda, B. Doshi, N. Guijarro, X. Min, C.-J. Tang, M. Sillanpää, K. Sivula, S. Wang, MIL-101(Fe)/g-C₃N₄ for enhanced visible-light-driven photocatalysis toward simultaneous reduction of Cr(VI) and oxidation of bisphenol A in aqueous media, *Appl. Catal. B: Environ.* 272 (2020), 119033.
- [18] Y. Gong, B. Yang, H. Zhang, X. Zhao, A g-C₃N₄/MIL-101(Fe) heterostructure composite for highly efficient BPA degradation with persulfate under visible light irradiation, *J. Mater. Chem. A* 6 (2018) 23703–23711.
- [19] S. Ding, S. Liu, J. Li, L. Wu, Z.F. Ma, X. Yuan, Multifunctional catalyst CuS for nonaqueous rechargeable lithium-Oxygen batteries, *ACS Appl. Mater. Interfaces* 13 (2021) 50065–50075.
- [20] Y. Li, Q. Zhao, Y. Zhang, Y. Li, L. Fan, F.-t Li, X. Li, In-situ construction of sequential heterostructured CoS/CdS/CuS for building “electron-welcome zone” to enhance solar-to-hydrogen conversion, *Appl. Catal. B: Environ.* 300 (2022), 120763.
- [21] Q. Chen, H. Zhou, J. Wang, J. Bi, F. Dong, Activating earth-abundant insulator BaSO₄ for visible-light induced degradation of tetracycline, *Appl. Catal. B: Environ.* 307 (2022), 121182.
- [22] C. Lai, M. Zhang, B. Li, D. Huang, G. Zeng, L. Qin, X. Liu, H. Yi, M. Cheng, L. Li, Z. Chen, L. Chen, Fabrication of CuS/BiVO₄ (0 4 0) binary heterojunction photocatalysts with enhanced photocatalytic activity for Ciprofloxacin degradation and mechanism insight, *Chem. Eng. J.* 358 (2019) 891–902.
- [23] X. Li, H. Liu, X. Jia, G. Li, T. An, Y. Gao, Novel approach for removing brominated flame retardant from aquatic environments using Cu/Fe-based metal-organic frameworks: a case of hexabromocyclododecane (HBCD), *Sci. Total Environ.* 621 (2018) 1533–1541.
- [24] J. Joseph, S. Iftikhar, V. Srivastava, Z. Fallah, E.N. Zare, M. Sillanpää, Iron-based metal-organic framework: Synthesis, structure and current technologies for water reclamation with deep insight into framework integrity, *Chemosphere* 284 (2021), 131171.
- [25] M.-W. Zhang, K.-Y.A. Lin, C.-F. Huang, S. Tong, Enhanced degradation of toxic azo dye, amaranth, in water using Oxone catalyzed by MIL-101-NH₂ under visible light irradiation, *Sep. Purif. Technol.* 227 (2019), 115632.
- [26] L. Benisek, Polarographic determination of isophthalic acid in the presence of terephthalic acid in polyester fibers, *Text. Res. J.* 32 (1962) 539–548.
- [27] A. Nose, T. Kudo, Reduction with sodium borohydride-transition metal salt systems. I. reduction of aromatic nitro compounds with the sodium borohydride-nickelous chloride system, *Chem. Pharm. Bull.* 29 (1981) 1159.
- [28] J. Qi, X. Yang, P.Y. Pan, T. Huang, X. Yang, C.C. Wang, W. Liu, Interface engineering of Co(OH)₂ nanosheets growing on the KNbO₃ perovskite based on electronic structure modulation for enhanced peroxymonosulfate activation, *Environ. Sci. Technol.* 56 (2022) 5200–5212.
- [29] Z. Lian, M. Sakamoto, H. Matsunaga, J.J.M. Vequizo, A. Yamakata, M. Haruta, H. Kurata, W. Ota, T. Sato, T. Teranishi, Near infrared light induced plasmonic hot hole transfer at a nano-heterointerface, *Nat. Commun.* 9 (2018) 2314.
- [30] X.-Y. Guo, J.-H. Guo, X.-Y. Zhang, S.-Q. Wang, X.-M. Cheng, W.-Y. Sun, Structure-dependent iron-based metal-organic frameworks for selective CO₂-to-CH₄ photocatalytic reduction, *J. Mater. Chem. A* 8 (2020) 25850–25856.
- [31] X.-Z. Song, F.-F. Sun, Y.-L. Meng, Z.-W. Wang, Q.-F. Su, Z. Tan, Hollow core-shell NiCo₂S₄@MoS₂ dodecahedrons with enhanced performance for supercapacitors and hydrogen evolution reaction, *New J. Chem.* 43 (2019) 3601–3608.
- [32] J. Cao, X. Li, X. Wang, K. Li, Y. Liu, H. Tian, Surface PEGylation of MIL-101(Fe) nanoparticles for co-delivery of radioprotective agents, *Chem. Eng. J.* 384 (2020), 123363.
- [33] Z. Wu, X. Liu, C. Yu, F. Li, W. Zhou, L. Wei, Construct interesting CuS/TiO₂ architectures for effective removal of Cr(VI) in simulated wastewater via the strong synergistic adsorption and photocatalytic process, *Sci. Total Environ.* 796 (2021), 148941.
- [34] K. Vinothkumar, M. Shivanna Jyothi, C. Lavanya, M. Sakar, S. Valiyaveetil, R. G. Balakrishna, Strongly co-ordinated MOF-PSF matrix for selective adsorption, separation and photodegradation of dyes, *Chem. Eng. J.* 428 (2022), 132561.
- [35] H. He, Y. Wang, J. Li, S. Jiang, S. Sidra, W. Gong, Y. Tang, Y. Hu, R. Wei, D. Yang, X. Li, Z. Zhao, Confined conductive and light-adsorbed network in metal organic frameworks (MIL-88B(Fe)) with enhanced photo-Fenton catalytic activity for sulfamethoxazole degradation, *Chem. Eng. J.* 427 (2022), 131962.
- [36] J. Ji, Q. Yan, P. Yin, S. Mine, M. Matsuoka, M. Xing, Defects on CoS_{2-x}: tuning redox reactions for sustainable degradation of organic pollutants, *Angew. Chem. Int. Ed.* 60 (2021) 2903–2908.
- [37] Y. Li, T. Chen, S. Zhao, P. Wu, Y. Chong, A. Li, Y. Zhao, G. Chen, X. Jin, Y. Qiu, D. Ye, Engineering cobalt oxide with coexisting cobalt defects and oxygen vacancies for enhanced catalytic oxidation of toluene, *ACS Catal.* (2022) 4906–4917.
- [38] Q. Yan, C. Lian, K. Huang, L. Liang, H. Yu, P. Yin, J. Zhang, M. Xing, Constructing an acidic microenvironment by MoS₂ in heterogeneous fenton reaction for pollutant control, *Angew. Chem. Int. Ed. Engl.* 60 (2021) 17155–17163.
- [39] Y. Ding, Y. Chen, Z. Guan, Y. Zhao, J. Lin, Y. Jiao, G. Tian, Hierarchical CuS@In₂S₄ hollow double-shelled p-n heterojunction octahedra decorated with fullerene C₆₀ for remarkable selectivity and activity of CO₂ photoreduction into CH₄, *ACS Appl. Mater. Interfaces* 14 (2022) 7888–7899.
- [40] L. An, Y. Li, M. Luo, J. Yin, Y.-Q. Zhao, C. Xu, F. Cheng, Y. Yang, P. Xi, S. Guo, Atomic-level coupled interfaces and lattice distortion on CuS/NiS₂ nanocrystals boost oxygen catalysis for flexible Zn-Air batteries, *Adv. Funct. Mater.* 27 (2017) 1703779.
- [41] Y. Liu, J. Qiao, Y. Sun, X. Guan, Simultaneous sequestration of humic acid-complexed Pb(II), Zn(II), Cd(II), and As(V) by sulfidated zero-valent iron: performance and stability of sequestration products, *Environ. Sci. Technol.* 56 (2022) 3127–3137.
- [42] M.-W. Zhang, K.-Y.A. Lin, C.-F. Huang, S. Tong, Enhanced degradation of toxic azo dye, amaranth, in water using Oxone catalyzed by MIL-101-NH₂ under visible light irradiation, *Sep. Purif. Technol.* 227 (2019), 115632.
- [43] Z.D. Lei, Y.C. Xue, W.Q. Chen, L. Li, W.H. Qiu, Y. Zhang, L. Tang, The influence of carbon nitride nanosheets doping on the crystalline formation of MIL-88B(Fe) and the photocatalytic activities, *Small* 14 (2018), e1802045.
- [44] Y. Wang, Q. Liu, N.H. Wong, J. Sunarso, J. Huang, G. Dai, X. Hou, X. Li, Near-infrared (NIR) light responsiveness of CuS/S-C₃N₄ heterojunction photocatalyst with enhanced tetracycline degradation activity, *Ceram. Int.* 48 (2022) 2459–2469.
- [45] B. Zhang, L. Zhang, K. Akiyama, P.A. Bingham, Y. Zhou, S. Kubuki, Self-assembly of nanosheet-supported Fe-MOF heterocrystals as a reusable catalyst for boosting advanced oxidation performance via radical and nonradical pathways, *ACS Appl. Mater. Interfaces* 13 (2021) 22694–22707.
- [46] L. Zhou, S. Dai, S. Xu, Y. She, Y. Li, S. Leveigneur, Y. Qin, Piezoelectric effect synergistically enhances the performance of Ti₃C₂-oxo-cluster/BaTiO₃/CuS p-n heterojunction photocatalytic degradation of pollutants, *Appl. Catal. B: Environ.* 291 (2021), 120019.
- [47] Q. Wang, P. Wang, P. Xu, Y. Li, J. Duan, G. Zhang, L. Hu, X. Wang, W. Zhang, Visible-light-driven photo-Fenton reactions using Zn_{1.5}Fe S/g-C₃N₄ photocatalyst: degradation kinetics and mechanisms analysis, *Appl. Catal. B: Environ.* 266 (2020), 118653.
- [48] L. Liao, Q. Zhang, Z. Su, Z. Zhao, Y. Wang, Y. Li, X. Lu, D. Wei, G. Feng, Q. Yu, X. Cai, J. Zhao, Z. Ren, H. Fang, F. Robles-Hernandez, S. Baldelli, J. Bao, Efficient solar water-splitting using a nanocrystalline CoO photocatalyst, *Nat. Nanotechnol.* 9 (2014) 69–73.
- [49] J. Liu, Y. Li, J. Ke, S. Wang, L. Wang, H. Xiao, Black NiO-TiO₂ nanorods for solar photocatalysis: Recognition of electronic structure and reaction mechanism, *Appl. Catal. B: Environ.* 224 (2018) 705–714.
- [50] Z. Zhu, H. Huang, L. Liu, F. Chen, N. Tian, Y. Zhang, H. Yu, Chemically bonded α -Fe₂O₃/Bi₄MO₃Cl dot-on-plate Z-scheme junction with strong internal electric field for selective photo-oxidation of aromatic alcohols, *Angew. Chem. Int. Ed. Engl.* 61 (2022), e202203519.
- [51] M.Y. Lu, Y.T. Chang, H.J. Chen, Efficient self-driven photodetectors featuring a mixed-dimensional van der Waals heterojunction formed from a CdS nanowire and a MoTe₂ flake, *Small* 14 (2018), e1802302.
- [52] J. Lin, Y. Liu, Y. Liu, C. Huang, W. Liu, X. Mi, D. Fan, F. Fan, H. Lu, X. Chen, SnS₂ nanosheets/H-TiO₂ nanotube arrays as a type II heterojunctioned photoanode for photoelectrochemical water splitting, *ChemSusChem* 12 (2019) 961–967.
- [53] Z. Wei, W. Wang, W. Li, X. Bai, J. Zhao, E.C.M. Tse, D.L. Phillips, Y. Zhu, Steering electron-hole migration pathways using oxygen vacancies in tungsten oxides to enhance their photocatalytic oxygen evolution performance, *Angew. Chem. Int. Ed.* 60 (2021) 8236–8242.
- [54] M. Rashid, D. Mowla, F. Esmailzadeh, K. Dashtian, M. Bahmani, Boosted Cr(VI) clean up over magnetically recoverable NiS/γ-Fe₂O₃/C type-II heterostructure derived from bimetal (Fe/Ni)-organic framework under visible light, *J. Clean. Prod.* 317 (2021), 128471.
- [55] H. Wang, T. Chen, D. Chen, X. Zou, M. Li, F. Huang, F. Sun, C. Wang, D. Shu, H. Liu, Sulfurized oolitic hematite as a heterogeneous Fenton-like catalyst for tetracycline antibiotic degradation, *Appl. Catal. B: Environ.* 260 (2020), 118203.
- [56] Q. Wu, J. Wang, Z. Wang, Y. Xu, Z. Xing, X. Zhang, Y. Guan, G. Liao, X. Li, High-loaded single Cu atoms decorated on N-doped graphene for boosting Fenton-like catalysis under neutral pH, *J. Mater. Chem. A* 8 (2020) 13685–13693.
- [57] Y. Ma, D. Xiong, X. Lv, X. Zhao, C. Meng, H. Xie, Z. Zhang, Rapid and long-lasting acceleration of zero-valent iron nanoparticles@Ti₃C₂-based MXene/

- peroxymonosulfate oxidation with bi-active centers toward ranitidine removal, *J. Mater. Chem. A* 9 (2021) 19817–19833.
- [58] O. Lorphensri, J. Intravijit, D.A. Sabatini, T.C. Kibbey, K. Osathaphan, C. Saiwan, Sorption of acetaminophen, 17 α -ethynyl estradiol, nalidixic acid, and norfloxacin to silica, alumina, and a hydrophobic medium, *Water Res.* 40 (2006) 1481–1491.
- [59] H. Liang, R. Liu, X. An, C. Hu, X. Zhang, H. Liu, Bimetal-organic frameworks with coordinatively unsaturated metal sites for highly efficient Fenton-like catalysis, *Chem. Eng. J.* 414 (2021), 128669.
- [60] H. Chen, Y. Xu, K. Zhu, H. Zhang, Understanding oxygen-deficient $\text{La}_2\text{CuO}_{4-\delta}$ perovskite activated peroxymonosulfate for bisphenol A degradation: The role of localized electron within oxygen vacancy, *Appl. Catal. B: Environ.* 284 (2021), 119732.
- [61] T. Cai, L. Wang, Y. Liu, S. Zhang, W. Dong, H. Chen, X. Yi, J. Yuan, X. Xia, C. Liu, S. Luo, $\text{Ag}_3\text{PO}_4/\text{Ti}_3\text{C}_2$ MXene interface materials as a Schottky catalyst with enhanced photocatalytic activities and anti-photocorrosion performance, *Appl. Catal. B: Environ.* 239 (2018) 545–554.
- [62] T. Wang, W. Liu, L. Xiong, N. Xu, J. Ni, Influence of pH, ionic strength and humic acid on competitive adsorption of Pb(II), Cd(II) and Cr(III) onto titanate nanotubes, *Chem. Eng. J.* 215–216 (2013) 366–374.
- [63] Y. Wu, X. Li, H. Zhao, F. Yao, J. Cao, Z. Chen, D. Wang, Q. Yang, Core-shell structured $\text{Cu}_2\text{O}/\text{HKUST-1}$ heterojunction photocatalyst with robust stability for highly efficient tetracycline hydrochloride degradation under visible light, *Chem. Eng. J.* 426 (2021), 131255.
- [64] Z. Li, F. Wang, Y. Zhang, Y. Lai, Q. Fang, Y. Duan, Activation of peroxymonosulfate by $\text{CuFe}_2\text{O}_4\text{-CoFe}_2\text{O}_4$ composite catalyst for efficient bisphenol A degradation: synthesis, catalytic mechanism and products toxicity assessment, *Chem. Eng. J.* 423 (2021), 130093.
- [65] A. Shahzad, J. Ali, J. Ifthikar, G.G. Aregay, J. Zhu, Z. Chen, Z. Chen, Non-radical PMS activation by the nanohybrid material with periodic confinement of reduced graphene oxide (rGO) and Cu hydroxides, *J. Hazard. Mater.* 392 (2020), 122316.
- [66] S. Xin, G. Liu, X. Ma, J. Gong, B. Ma, Q. Yan, Q. Chen, D. Ma, G. Zhang, M. Gao, Y. Xin, High efficiency heterogeneous Fenton-like catalyst biochar modified CuFeO_2 for the degradation of tetracycline: economical synthesis, catalytic performance and mechanism, *Appl. Catal. B: Environ.* 280 (2021), 119386.
- [67] C. Peng, G. Luo, J. Zhang, M. Chen, Z. Wang, T.K. Sham, L. Zhang, Y. Li, G. Zheng, Double sulfur vacancies by lithium tuning enhance CO_2 electroreduction to n-propanol, *Nat. Commun.* 12 (2021) 1580.
- [68] Z. Zhang, Y. Zhu, X. Chen, H. Zhang, J. Wang, A. Full-Spectrum, Metal-free porphyrin supramolecular photocatalyst for dual functions of highly efficient hydrogen and oxygen evolution, *Adv. Mater.* 31 (2019), e1806626.
- [69] X. Hu, X. Peng, L. Kong, Mechanism for Photopromoted Release of Vanadium from Vanadium Titano-Magnetite, *Environ. Sci. Technol.* 52 (2018) 1954–1962.
- [70] Y. Yang, Q. Wang, R. Aleisa, T. Zhao, S. Ma, G. Zhang, T. Yao, Y. Yin, MoS_2/FeS nanocomposite catalyst for efficient fenton reaction, *ACS Appl. Mater. Interfaces* 13 (2021) 51829–51838.
- [71] T. Lu, F. Chen, Multiwfn: a multifunctional wavefunction analyzer, *J. Comput. Chem.* 33 (2012) 580–592.
- [72] J. Qi, J. Liu, F. Sun, T. Huang, J. Duan, W. Liu, High active amorphous $\text{Co}(\text{OH})_2$ nanocages as peroxymonosulfate activator for boosting acetaminophen degradation and DFT calculation, *Chin. Chem. Lett.* 32 (2021) 1814–1818.
- [73] Y. Bao, C. Lian, K. Huang, H. Yu, W. Liu, J. Zhang, M. Xing, Generating high-valent iron-oxo identical with $\text{Fe}(\text{IV})=\text{O}$ complexes in neutral microenvironments through peroxymonosulfate activation by Zn-Fe layered double hydroxides, *Angew. Chem. Int. Ed.* (2022), e202209542.